



Graphene as Vehicle for Ultrafast Lithium Ion Capacitor Development Based on Recycled Olive Pit Derived Carbons

Jon Ajuria,^{1,z} Mainer Zarrabeitia,^{2,a} María Arnaiz,^{1,2} Oxel Urra,¹ Teófilo Rojo,^{1,2} and Eider Goikolea^{2,z}

¹CIC Energigune, Albert Einstein 48, Technology Park of Alava, 01510, Vitoria-Gasteiz, Spain

²Inorganic Chemistry Department, University of the Basque Country UPV/EHU, 48080 Bilbao, Spain

Herein we report a series of lithium ion capacitors (LICs) with extraordinary energy-to-power ratios based on olive pit recycled carbons and supported on graphene as a conducting matrix. LICs typically present limited energy densities at high power densities due to the sluggish kinetics of the battery-type electrode. To circumvent this limitation, the hard carbon (HC) was embedded in a reduced graphene oxide (rGO) matrix. The addition of rGO into the negative electrode not only forms a 3D interpenetrating carbon network but also wraps HC particles, facilitating ion diffusion and enhancing the electronic conductivity notably at high power densities. Electrochemical impedance spectroscopy (EIS) analysis reveals that charge-transfer resistance at electrode-electrolyte interphase and the charge-transport resistance within the electrode are considerably lower in the presence of rGO. In addition, charge-transport resistance remains constant upon cycling even at increasing current densities. Capacity gain at high current densities, owing to the reduction of the electrode resistance, triggers the overall LIC performance, allowing for the assembly of an ultrafast LIC delivering up to 200 Wh kg⁻¹ at low power rates and 100 Wh kg⁻¹ at a power of 10 kW kg⁻¹.

© The Author(s) 2019. Published by ECS. This is an open access article distributed under the terms of the Creative Commons Attribution 4.0 License (CC BY, <http://creativecommons.org/licenses/by/4.0/>), which permits unrestricted reuse of the work in any medium, provided the original work is properly cited. [DOI: 10.1149/2.0361913jes]



Manuscript submitted June 11, 2019; revised manuscript received July 18, 2019. Published August 21, 2019.

Lithium ion batteries (LIBs) and supercapacitors (SCs) have been mostly adopted solutions for electrical energy storage (EES) in many fields.¹ Nevertheless, in view of the growing demand of applications that are calling for high energy density at high power ratios, lithium ion capacitors (LICs) are now in vogue among diverse, but all trailblazing industries -i.e. consumer electronics, automotive or aerospace-. Their ability to provide high energy densities at high power densities has attracted a big deal of attention, making this technology highly eye-catching for many areas, from academia to industry. Thus, LICs are becoming promising candidates to enter the exclusive EES club.²

LICs were first demonstrated in 2001, based on the idea of increasing the energy density of an electric double-layer capacitor (EDLC) by replacing the carbonaceous negative electrode with a lithium titanate (Li₄Ti₅O₁₂) -a lithium ion insertion material- in order to increase the overall capacity.³ Significant progress was achieved shortly after, when graphite was introduced as negative electrode, since its low working potential (~0.1 V vs. Li⁺/Li) allowed to widen the operative window voltage of the LIC up to 4.2 V.⁴ In fact, owing to its excellent features such as, low working potential, low-cost, good cycle life and a high theoretical gravimetric capacity of 372 mAh g⁻¹, LIC technology reached the market in 2008.⁵ In the last years, research has been focused on the battery-type electrode due to the sluggish kinetic of lithium-intercalation in comparison to the double-layer formation on the surface of the capacitor-type activated carbon (AC) electrode.⁶

In this context, hard carbons (HCs) are a promising alternative to graphite. Owing to their non-graphitizable disordered nature, lithium ion can intercalate at both sides of graphene sheets allowing targeting twice the theoretical capacity of graphite. In fact, HCs with higher capacity values, rate capabilities and longer cycling life have been widely reported.^{7,8} In addition, their faster kinetics with respect to graphite have turned HCs in one of the most studied type of anode material in LICs. Although most of the HC-based LICs reported to date show the capacity to operate almost at the SC power regime, it is upon loss of most of the energy gained owing to the hybridization.^{9,10} Usually, the poor energetic performance at those high power ratios is mainly ascribed to the slow kinetics of the HC with respect to the AC.¹¹ Though, we firmly believe that the crux of the matter relies on the electrode engineering, i.e. the formulation and fabrication process of the electrode, since both intrinsic ion diffusion and electronic con-

ductivity values of most HCs should in general be sufficiently high as to, at least, partially mimic the behavior of EDLCs at high power rates.

HCs can be synthesized from a wide variety of precursors, such as sucrose, cellulose, polyvinyl (PVC), furfuryl alcohol or even better, from sustainable resources like recycled biomass.¹²⁻¹⁹ The precursor, together with the pyrolysis temperature and activation process will determine the inherent micro and macroporous structure of the HC, and, accordingly, the ability to store charge. However, only an optimum electrode formulation will enable to get the most out of the material. Well studied factors such as particle morphology, carbon coating, electrode thickness, binder or electrolyte affect rate capability and cyclability of the HC.²⁰⁻²³ Certainly, key parameters such as charge-transfer resistance and the interparticle contact resistance (i.e. charge-transport) strongly depend on the configuration of the electrode. Currently, this problematic is mitigated by coating the HC particle surface with a highly conducting carbon. This is an effective solution for batteries that work at low cycling rates but not applicable to LICs, where the applied current density is highly demanding, and this approach is unable to keep a reasonable rate capability.^{24,25} Thus, the HC electrode needs to be tailored for its application in LIC technology. To this end, a strategy to improve conductivity and rate capability of HC electrodes based on the addition of thermally exfoliated reduced graphene oxide (rGO) as a conducting agent has been adopted. Previously reported researches for advanced intercalation cathode materials, such as LiFePO₄ or Li₃V₂(PO₄)₃, already showed satisfactory increase on the capacity and rate capability.^{26,27} However, few studies focused on anode materials have been reported to date. In addition, despite already reported HC-graphene composites have achieved promising results in terms of electrode performance, they all present rather unattractive intricate synthesis route.²⁸ Besides, in most cases the electrochemical performance is limited to half-cells. In this work, the aim is to replace the standard conducting carbon coating with a rGO matrix, tailoring the electrochemical properties of the HC electrode and enabling its implementation in a final LIC device without any power penalization. In fact, by a simple physical mixing, HC particles have been embedded into a highly conducting 3D interconnecting graphene network that acts as a pathway for both ion diffusion and electron transport. As a result, electrochemical performance is greatly enhanced at high rates, e.g. at 10C rate, where capacity gain is more than 100% owing to a substantial charge-transfer and charge-transport resistance attenuation. Further implementation of the HC-rGO electrode into a LIC becomes a game changer, enabling a final device with an ultrafast response reaching even higher power values than its EDLC counterpart.

^aPresent address: Helmholtz-Institute Ulm (HIU), Helmholtzstrasse 11, 89081, Ulm and Karlsruhe Institute of Technology (KIT), P.O. Box 3640, 76021, Karlsruhe, Germany.

^zE-mail: jajuria@cicenergigune.com; eider.goikolea@ehu.es

Experimental

Material synthesis.—To prepare the HC, olive pits were crushed after received and loaded in a tubular furnace for the pyrolysis process by heating under an Ar flow of 100 ml min⁻¹ at a ramp rate of 5°C min⁻¹ to a predefined temperature of 900°C and further holding it for 2 hours (the carbonization yield for olive pits was ~25%). A similar HC was previously prepared and studied by our group,²⁵ however, with the aim of enlarging crystallites and, ultimately, reduce the irreversibility of the first cycle, in this work the pyrolysis temperature was slightly increased.

To prepare the AC, the HC obtained from the pyrolysis of raw olive pits at 700°C was physically mixed with potassium hydroxide, KOH, in a C/KOH 1/6 mass ratio. The mixture was placed in an Inconel boat and activated according to the procedures described in the literature, i.e. heating up to the maximum temperature under an Ar flow (100 ml min⁻¹) inside a horizontal stainless steel tube within a tubular furnace. The heating ramp rate was 5°C min⁻¹ and the holding time at 700°C was 2 hours. After activation, the microporous AC was washed off with a diluted solution of hydrochloric acid, HCl (aq), and water until neutral pH was reached and then dried at 120°C under vacuum (the activation yield was ~75%).

To prepare the rGO, first graphite oxide was obtained from the synthetic graphite provided by Timalc (TIMREX-SFG75) by a previously reported modified Hummers' method.²⁹ Subsequent, a rapid heating (>1000°C min⁻¹) to 1000°C splits the graphite oxide into individual graphene oxide (GO) sheets.³⁰ Finally, GO sheets were thermally treated at 1°C min⁻¹ to 250°C to avoid disordering of GO layers and at 2°C min⁻¹ to 650°C for 1 hour under Ar atmosphere (100 ml min⁻¹) in order to obtain the rGO samples.

Material characterization.—N₂ adsorption/desorption isotherms were measured at -195.8°C using a Micromeritics ASAP 2020 instrument for relative pressure values (P/P₀) between 10⁻⁸ and 0.995 for samples preliminarily outgassed for 24 hours at 200°C. The Specific Surface Area (SSA) values were calculated by applying the recently-developed 2D Non-Local Density Functional Theory (2D NLDFT) treatment to N₂ adsorption/desorption isotherms using the data reduction software SAIEUS. X-ray diffraction (XRD) patterns were recorded for powdered samples in a Bruker Discover D8 X-ray diffractometer; data was collected at 40 kV and 30 mA using CuK α (1.5405 Å) radiation over a 2 θ range within 15 to 80°. Microstructure of carbons was characterized using Scanning Electron Microscope (SEM) FEI Quanta 200 FEG and Transmission Electron Microscope (TEM) FEI Tecnai G2 F20. X-ray Photoelectron Spectroscopy (XPS) measurements were carried out in a UHV spectrometer chamber with base pressure below 10⁻¹⁰ mbar. The chamber features a hemispherical analyzer PHOIBOS 150 with a 2D-DLD detector (SPECS) and monochromatic X-ray source FOCUS 500 (SPECS) with two anodes: Al K α (h ν $\frac{1}{4}$ 1486.74 eV) and Ag L α (h ν $\frac{1}{4}$ 2984.3 eV). Conductivity measurements were carried out by the four-probe Van der Pauw's method using the electrodes employed for the electrochemical measurements.

Electrode fabrication, LIC assembly and electrochemical characterization.—The slurries for the negative electrodes were prepared by mixing HC either with Super C65 (Imerys Graphite & Carbon) carbon black or with as-prepared rGO (no additional Super C65 in this case) to fabricate (i) the benchmark electrode, denoted by HC, and the new (ii) HC-rGO electrodes, respectively. Polyvinylidene fluoride (PVdF) was used as the binder in a mass ratio of 5% in all cases. The formulation of each electrode is summarized in Table I. For the positive electrode, the slurry was prepared by mixing the AC and PVdF in a mass ratio of 95:5. After adding N-methyl-2-pyrrolidone (NMP), slurries were mixed under vigorous stirring for 1 hour. HC slurries were deposited onto copper current collector sheets whereas the AC slurry was laminated onto an aluminum current collector sheet. Laminates were immediately transferred into a vacuum oven and dried at

Table I. Formulation of the three electrodes studied.

Name/Formulation	HC	SuperC65	rGO	PVdF
HC	90	5	-	5
HC-rGO-2	93	-	2	5
HC-rGO-5	90	-	5	5

80°C under constant vacuum for 12 hours before 1 cm² circular individual electrodes were cut out. All electrodes weighed around 1 mg cm⁻² with a thickness about 30 microns and 50 microns for the HCs and ACs respectively. Before the cell assembly, all electrodes were dried at 120°C overnight in a vacuum oven. Prior to the assembly of full hybrid cells, HC-based electrodes were characterized in a three-electrode Swagelok airtight system using metallic lithium, both as the counter and reference electrodes and 1 M LiPF₆ in EC:DMC (1:1; v/v; ethylene carbonate: dimethyl carbonate) as electrolyte. Reported capacities always refer to the HC mass (mg of HC). LICs were assembled in a three-electrode Swagelok system with lithium metal as a reference, using stainless steel current collectors and a porous fiber glass (Whatman GFB) membrane separator in the same electrolyte as in half-cells, 1 M LiPF₆ in EC:DMC. Reported values always refer to the sum of the active mass (AM) of both electrodes (mg of HC + mg of AC). Cyclic voltammetry (CV), galvanostatic (GA) charge/discharge cycling and electrochemical impedance spectroscopy (EIS) measurements were conducted using a multichannel VMP3 generator (Biologic, France) at room temperature (i.e. 21°C) applying a low sinusoidal amplitude alternating voltage of 10 mV over zero current potential (OCP) at frequencies from 1 MHz to 10 mHz at 0.2 V vs. Li⁺/Li after discharging at three different current densities: C/10, 1C, 10C. The EIS data was fitted using Boukamp's software.³¹

Results and Discussion

On the search for a highly conducting graphene, the choice for a thermally exfoliated rGO is done in view of the low presence of oxygen achieved,³² which is directly related to its electronic conductivity.³³ The XRD pattern shown in Fig. 1a, with a broad (002) diffraction peak at 26.1°, is indicative of the partially ordered structure of rGO with a similar interplanar spacing but lower crystallinity than graphite (resulting d₀₀₂ = 3.31 Å and L_c = 5.6 nm). Further structural analysis carried out by Raman spectroscopy (Fig. 1b) confirmed the disordered morphology and low degree of graphitization of the obtained rGO. The Raman spectrum shows a G-band at ~1580 cm⁻¹ (in-plane C-C vibrations) and a D-band at ~1340 cm⁻¹ (a breathing mode only active when there is disorder in the structure) and two broad peaks in the region 2500–3000 cm⁻¹ corresponding to 2D and D+G bands. The ratio between the integrated peak areas of I_D and I_G bands turned out to be 1.24 in good agreement with the disordered nature of rGO. The presence of corrugated single layers of graphene is confirmed by means of TEM imaging (Fig. 1c) and the typical agglomerated fluffy appearance of graphene can also be observed by SEM (Fig. 1d). The SSA of rGO was calculated from the N₂ adsorption isotherm (Fig. 1e). The isotherm analyzed by Brunauer–Emmett–Teller (BET) method reports a SSA of 1042 m² g⁻¹ while using the 2D NLDFT treatment the final SSA is 742 m² g⁻¹ (Fig. 1f). Furthermore, the oxygen content confirmed by XPS is as low as 3%, allowing to target a high conductivity of 747 S cm⁻¹ which is one order of magnitude higher than that measured for the AC (41 S cm⁻¹). All the physicochemical data is summarized in Table II.

The microstructural characterization of the benchmark HC electrode and the newly developed HC-rGO-5 electrode reveals considerable differences at first sight. On one side, HC-rGO-5 electrode seems to be highly permeable, with an open structure at the microscale (Fig. 2a), allowing for a straightforward electrolyte propagation through the electrode toward HC particles, an essential requirement for fast operation at high power demand. On the other

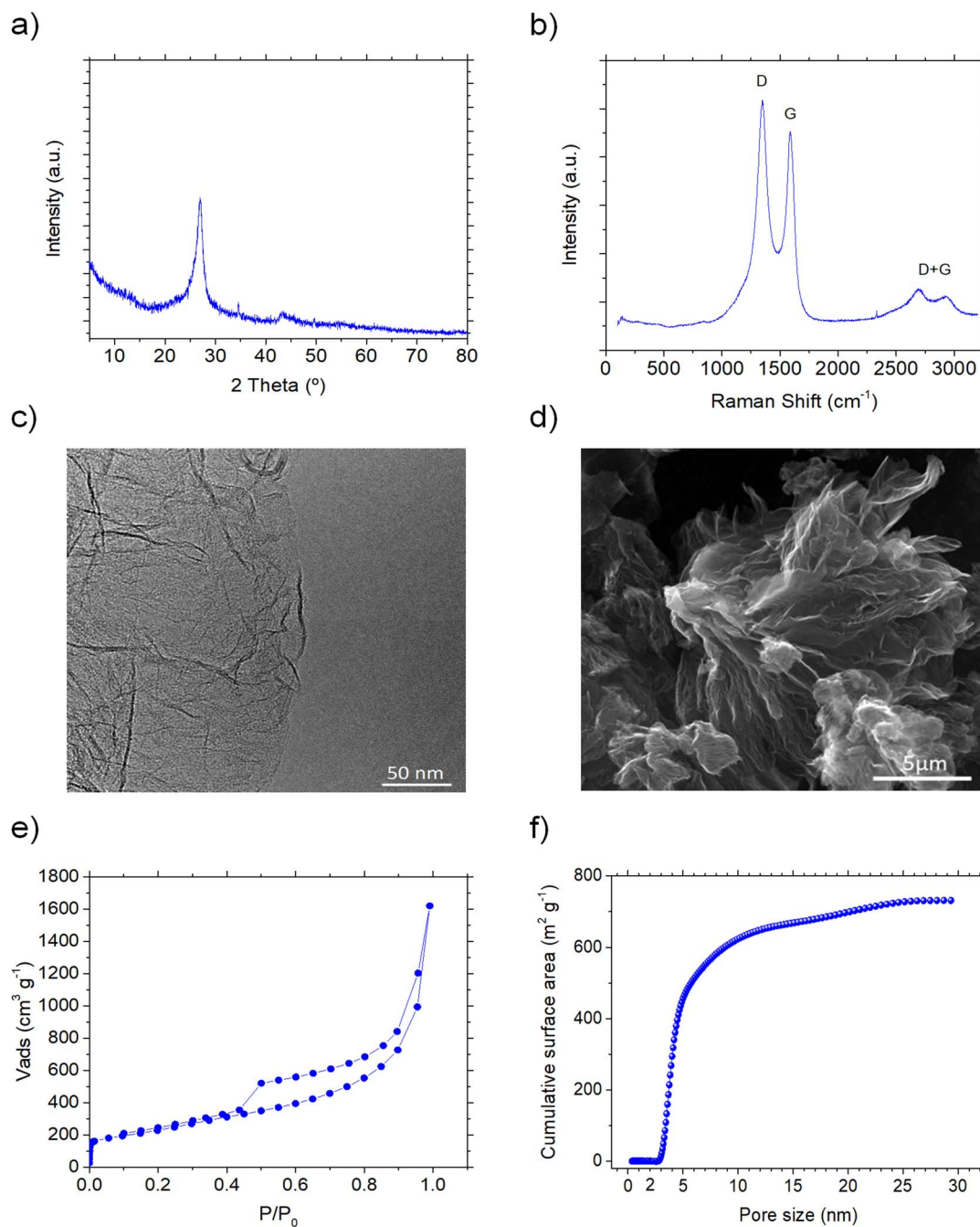


Figure 1. Physicochemical characterization of rGO: a) XRD pattern, b) Raman Spectrum, c) TEM micrograph, d) SEM micrograph, e) N_2 adsorption/desorption isotherm and f) Cumulative surface area calculated using 2D-NLDFT.

side, the HC electrode (Fig. 2b) shows a more closed appearance, probably implying a more tortuous route for electrolyte propagation. The more open structure of HC-rGO-5 vs. HC is clearly confirmed at higher magnifications (Figs. 2c vs. 2d). Although the 3D nature of graphene begins to glimpse at this point, further magni-

fications (Fig. 2e) confirm that HC particles are clearly embedded into a 3D rGO matrix that interconnects particles, theoretically providing enhanced ion diffusion and electron transport paths.³⁴ In addition, Fig. 2f shows in more detail how the rGO matrix not only bridges particles but also wraps them, providing a quasi-continuous

Table II. Experimental physicochemical data obtained for rGO.

	SSA		XRD		Raman I_D/I_G	XPS		Conductivity ($S\ m^{-1}$)
	DFT ($m^2\ g^{-1}$)	BET ($m^2\ g^{-1}$)	Lc(nm)	d_{002} (Å)		C (%at)	O (%at)	
rGO	742	1042	5.6	3.31	1.24	97	3	747

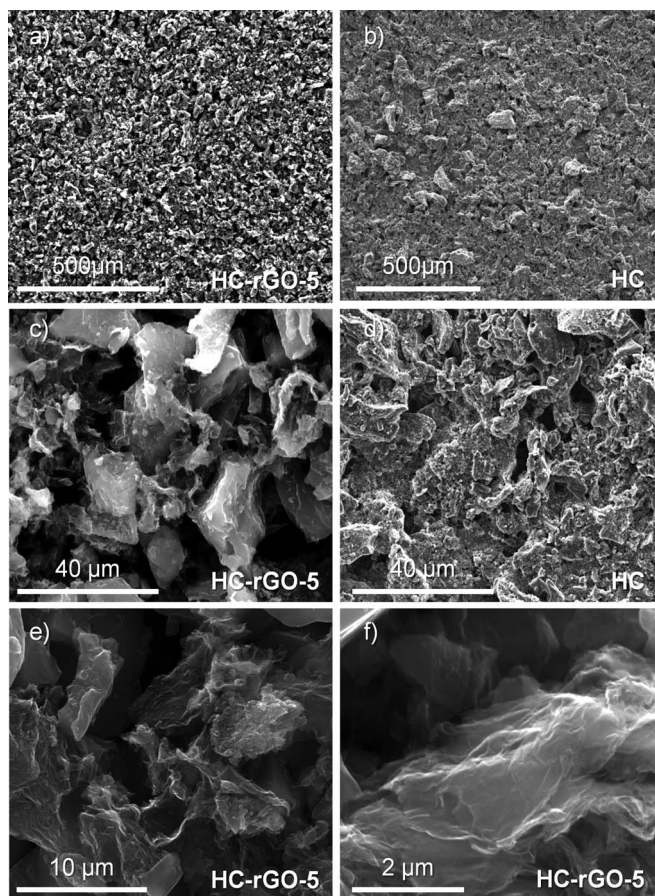


Figure 2. SEM micrographs of a) c) e) and f) HC-rGO-5 electrode and b) and d) HC electrode at different magnifications.

path along the particles for both electrons and ions to be transferred and transported.

GA charge/discharge experiments for HC and HC-rGO electrodes were carried out in the potential range of 0.005–2 V vs. Li^+/Li at different current densities between C/10 and 10C, being $C = 372 \text{ mAh g}^{-1}$. As observed in Figs. 3a and 3b, charge/discharge profiles are very similar for both electrodes, and consist of a slopy region and a plateau at low potential. Attending to the “house of cards” model, ions are intercalated into the interlayer between graphene sheets along the slopy region until ca. 0.2 V vs. Li^+/Li , while below this potential a plateau appears owing to reversible insertion of lithium ion into nanopores.³⁵ Olive pit derived HCs show better storage capabilities at the slopy region than at the low potential plateau owing to the intrinsic nature and composition of the precursor material. For safety reasons, this is a highly desired feature of this technology. Indeed, when building LICs, the cut-off potential of the negative electrode is limited to 0.1 V vs. Li^+/Li to avoid any lithium plating, disabling the access to the capacity stored below this potential. Therefore, the higher is the capacity of the electrodes above this potential, the better the system will perform. Undoubtedly, the replacement of C65 by means of rGO contributes to the electrode capacity due to the lithium storage within the graphene layers. In order to estimate this contribution, a fully rGO based electrode was electrochemically characterized and GA charge/discharge profiles are shown in Fig. 3c. After five stabilization cycles at a C/10 discharge rate, rGO exhibits a maximum capacity of 266 mAh g^{-1} , which is practically equal to the capacity delivered by the HC electrode (275 mAh g^{-1}). Since capacity values of both materials seem to be quite similar at all studied discharge rates, and attending to the composition of the HC-rGO-5 electrode (90% HC, 5% rGO), it can be concluded that the rGO contribution to the charge storage capacity

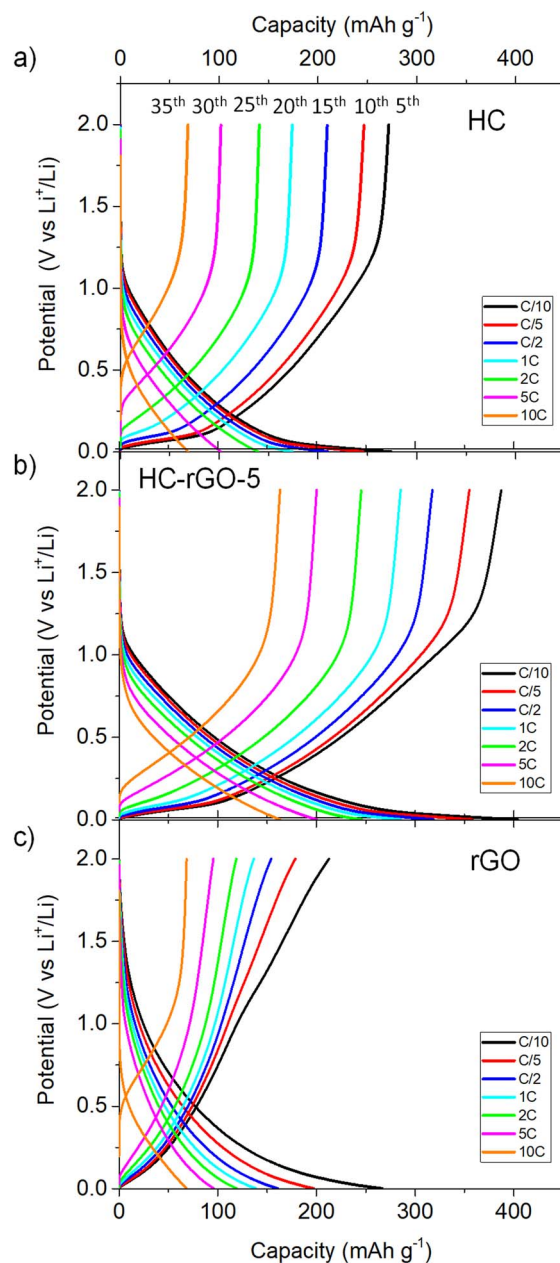


Figure 3. GA charge/discharge profiles of a) HC b) HC-rGO-5 and c) bare rGO electrodes between 0.005–2 V vs. Li^+/Li .

is about 5%. Nevertheless, the improved performance of the HC-rGO electrode goes beyond the capacity contribution of rGO, and might be related to a synergistic effect of the HC and rGO combination.

Rate capability data for the HC electrode together with the HC-rGO electrodes is summarized in Fig. 4a. At C/10, the HC electrode shows a reversible capacity of 275 mAh g^{-1} , while the irreversible capacity of the first cycle is 175 mAh g^{-1} , limiting the initial Coulombic efficiency (CE) to 61%. Along the increasingly applied current densities, capacity fades to 175 mAh g^{-1} at 1C, and continues downwards to reach ca. 70 mAh g^{-1} at high current densities (i.e. 10C), that is, only 25% of retention of the initial reversible capacity. Replacement of C65 by means 5% of rGO boosts the capacity of the HC-rGO-5 electrode through all over the discharge times. As expected, CE of the first cycle is lowered to 56% due to the larger active surface of the electrode after the rGO addition, which enlarges solid electrolyte interphase (SEI) formation. On the other hand, the reversible capacity of HC-rGO-5 boosts to 450 mAh g^{-1} , that is a 60% increase respect the initial HC

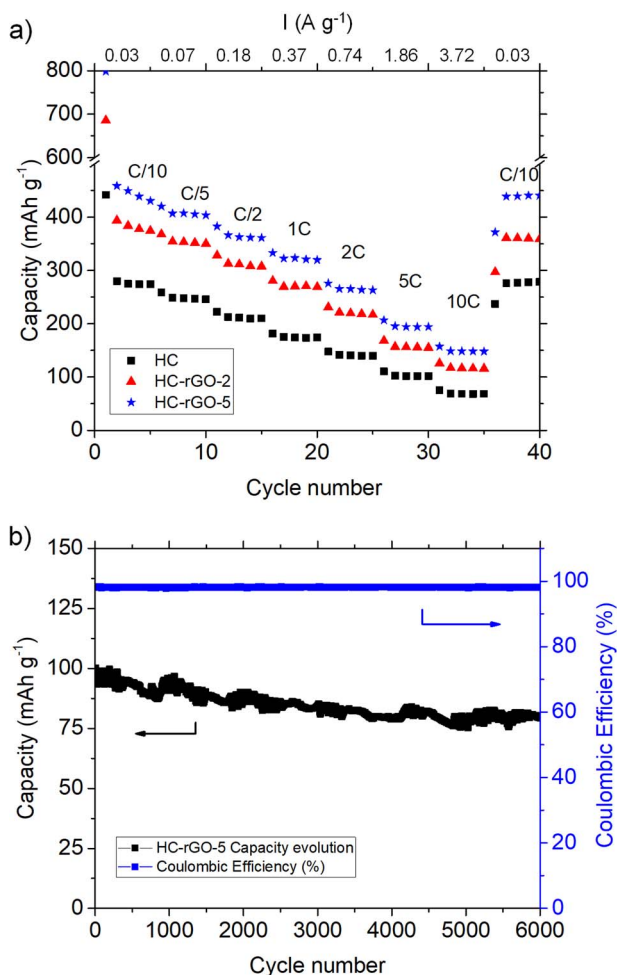


Figure 4. a) Rate capability of the HC (black square), HC-rGO-2 (red triangle) and HC-rGO-5 (blue star) and b) Stability test for HC-rGO-5 at 10C.

electrode. Capacity retention at 10C rises to 35%, improving that of the benchmark electrode in 10 percentage points, i.e. more than a 2-fold increase, reaching a capacity value of 162 mAh g^{-1} . In order to further evaluate the impact of rGO within the electrode performance, an intermediate electrode composition was also characterized by using only 2% of rGO in the formulation. First reversible discharge cycle offers a capacity of 400 mAh g^{-1} at C/10 (CE of 57%), which implies a 45% rise with respect to the HC electrode but is still far from the 60% gain achieved by the addition of 5% of rGO. Capacity retention at 10C is 29%, delivering 115 mAh g^{-1} , that is 45 mAh g^{-1} more than the benchmark HC electrode but 47 mAh g^{-1} less than the HC-rGO-5 electrode. In view of these results, HC-rGO-5 was selected to be implemented in the LIC system while HC-rGO-2 was discarded. Since cyclability is a major strength of SCs technology, HC-rGO-5 electrode was exposed to a cycle life test (Fig. 4b). The upper potential window of the electrode was set to 2 V vs. Li^+/Li while the lower potential was set as for the operational conditions within the LIC (that is, limiting the lower potential to 0.1 V vs. Li^+/Li) and cycled at a 10C rate ($t_{\text{discharge}} = \sim 47$ seconds). At this high discharge rate CE is $\geq 98\%$, thus some degradation is expected to occur. Establishing the experiment end-point at capacity retention of 80%, the electrode is able to work for over 6000 cycles at those conditions. Since potential window used in the final LIC system will still be narrower, cycle life is expected to be even longer.

In order to better understand the impact of the added 5% of rGO within the overall capacity gain and with the aim to discern its role, EIS studies were carried out in both HC-rGO-5 and benchmark HC electrodes at the lowest working potential, (0.2 V vs. Li^+/Li), where the

Table III. Resistance values for HC and HC-rGO-5 electrodes at 0.2 V vs. Li^+/Li calculated using the equivalent circuit model by Boukamp's software at C/10, 1C and 10C rates.

C rate	HC			HC-rGO-5		
	C/10	1C	10C	C/10	1C	10C
R_{el} ($\text{Ohm}\cdot\text{cm}^2$)	2.3	2.3	2.3	1.2	1.2	1.2
R_{SEI} ($\text{Ohm}\cdot\text{cm}^2$)	1.3	1.9	1.4	0.2	0.5	0.4
R_{CT} ($\text{Ohm}\cdot\text{cm}^2$)	47.1	47.3	43.9	24.7	13.9	12.1
R_e ($\text{Ohm}\cdot\text{cm}^2$)	17.8	25.8	50.2	7.1	4.6	4.7
Chi^2	$1.1 \cdot 10^{-3}$	$7.4 \cdot 10^{-4}$	$8.0 \cdot 10^{-4}$	$6.4 \cdot 10^{-4}$	$7.9 \cdot 10^{-4}$	$7.2 \cdot 10^{-4}$

maximum functional Li^+/Li insertion within the electrode is achieved. The equivalent circuit (EC) used to fit EIS data was the same for both electrodes (top of Fig. 5). The EC consists on a resistance (R_{el}) connected in series to other three resistances (R_{SEI} , R_{CT} and R_e) each with their own constant phase element (CPE) connected in parallel and a semi-infinite Warburg impedance (Z_w) together with a pseudo-capacitance component (C_{int}). Since the electrodes do not follow an ideal behavior because of surface inhomogeneity, roughness etc, CPEs were used for the fits instead of capacities. This EC is a modification of the EC proposed by Aurbach and co-workers, which is considered the most accurate circuit for intercalation electrodes.³⁶⁻³⁸ According to Aurbach and co-workers, the intercept with the real axis ($Re Z$) corresponds mainly to ion resistance in the electrolyte and separator (R_{el}). As expected, R_{el} value, calculated from the EC, is very similar for both systems (Table III), since the same electrolyte was used, and mainly contributes to the potential (ohmic) drop of the system. At high/medium frequency (1 MHz to ~ 50 Hz for HC and 1 MHz to 2.5 Hz for HC-rGO-5) both electrodes present one big semicircle which encompasses at least two smaller semicircles. The diameter of the overall semicircle is much smaller for the HC-rGO-5 electrode, suggesting that it has lower resistance values. The first small semicircle at the highest frequency (not visible at the naked eye but necessary for the correct fit of the impedance) accounts for lithium ion transport through the SEI layer, that is fitted using a parallel EC consisting of a resistance (R_{SEI}) and a CPE (CPE_{SEI}). A second semicircle within the middle frequency range (600–400 Hz) accounts for the charge-transfer resistance at the electrode/electrolyte interface, that is fitted using a parallel EC consisting of a resistance (R_{CT}) and a CPE owing to the formation of the double-layer at the electrode/electrolyte interface (CPE_{DL}). Firstly, R_{SEI} turns out to be slightly smaller for the HC-rGO-5 electrode (Table III), due to the higher SSA of rGO (R_{SEI} is inversely proportional to SSA).³⁹ Secondly, R_{CT} values calculated using the EC (Table III) evident first significant differences since, the HC-rGO-5 electrode presents much lower resistance values. This suggests that the lithium ion insertion is easier when C65 is substituted by rGO. The lower R_{SEI} and R_{CT} values for the HC-rGO-5 might arise due to a smoother interface that results from wrapping HC particles in rGO. At the low frequency range, yet above 1 Hz, another semicircle appears in the HC electrode, and it is attributed to electron transport mechanisms through the overall electrode, in other words, to the electronic conductivity of the electrode. This process is fitted using a parallel circuit consisting of a resistance (R_e) with a CPE. This semicircle has already been observed in other intercalation materials.⁴⁰⁻⁴⁴ While HC electrode clearly shows a semicircle at low frequency (from ~ 25 Hz to ~ 0.5 Hz) HC-rGO-5 electrode does not exhibit any semicircle at the naked eye. Indeed, the semicircle corresponding to the electron transport mechanisms in HC-rGO-5 is overlapped with the big semicircle, which is centred around 270 Hz and it is only possible to identify fitting the EIS data. The almost absence of that process suggests that the electronic conductivity is increased by the addition of rGO within the HC-rGO-5 electrode. R_e values calculated from the EC give important insight about the rGO impact within the electrode performance. From one side, the HC electrode presents increasing R_e values through the increasingly applied C-rates. R_e rises from 18 to $50 \Omega \text{ cm}^2$ when C-rate

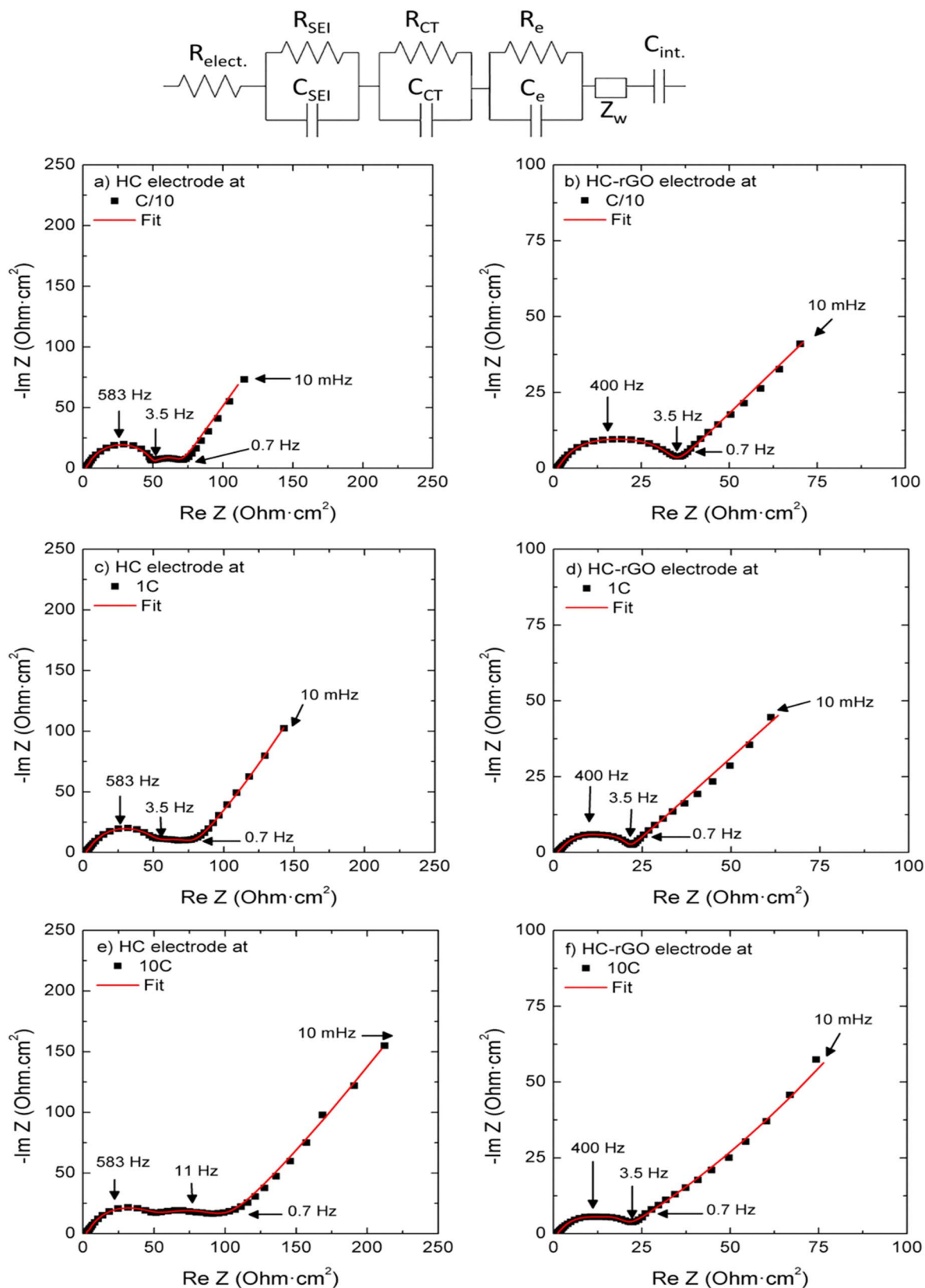


Figure 5. Equivalent circuit model on the top and Nyquist plots for a), c), e) HC and b), d), f) HC-rGO-5 electrodes at 0.2 V vs. Li^+/Li measured at C/10, 1C and 10C rates, respectively.

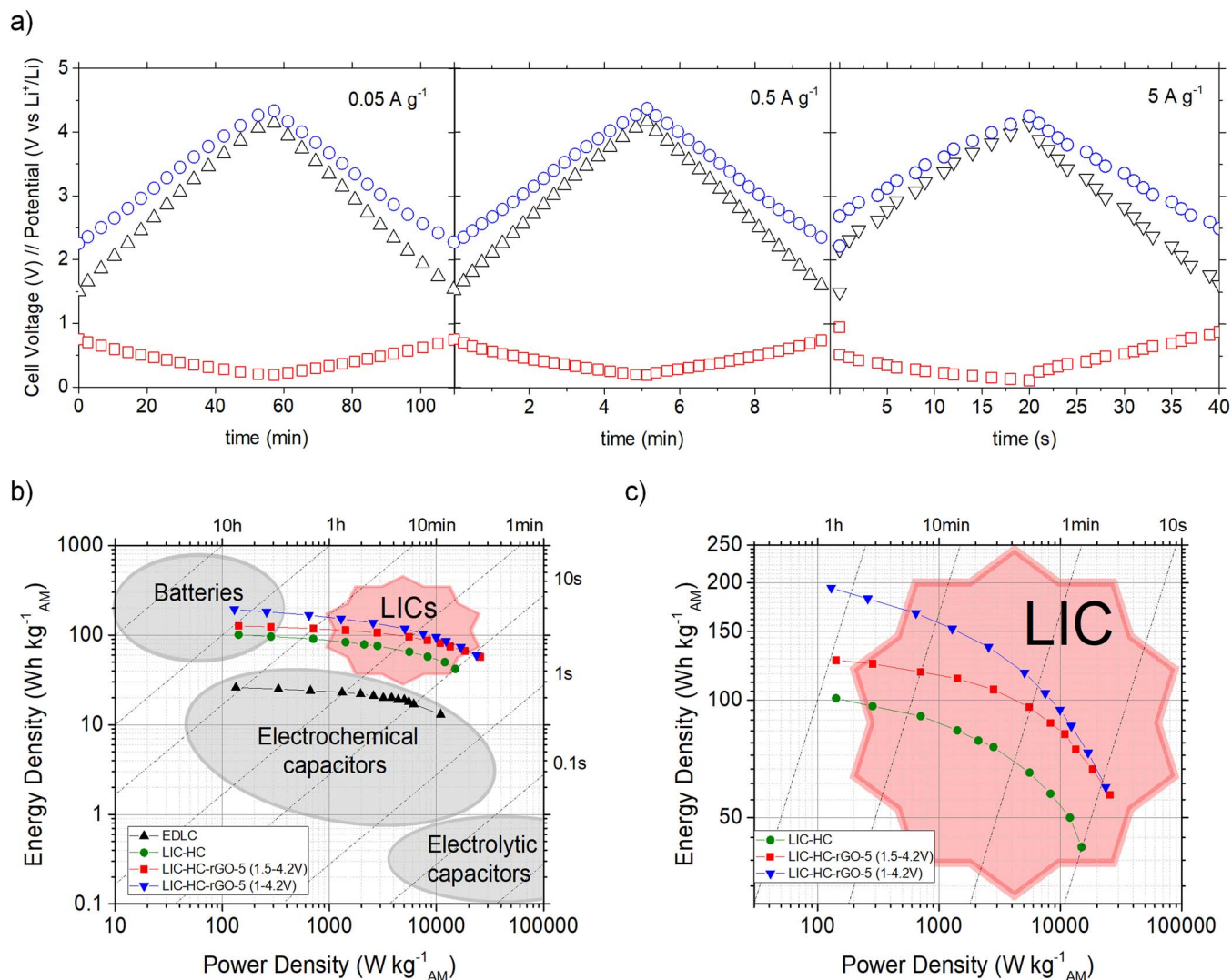


Figure 6. a) GA charge/discharge voltage profiles of HC-rGO-5:AC based LIC (black triangles) at applied 0.05, 0.5 and 5 A g⁻¹ current densities and their respective HC-rGO electrode (red squares) and AC electrode (blue circles) potentials vs. Li⁺/Li. b) Ragone Plot and c) Magnification of LICs region in the Ragone Plot.

is increased from C/10 to 10C. On the other side, within the HC-rGO-5 electrode R_c value remains almost constant and substantially lower, 7.1 and 4.7 $\Omega \text{ cm}^2$ at C/10 and 10C respectively. All these results provide clear evidence of the rGO impact onto the charge-transfer resistance reduction but especially onto the electronic conductivity. The substitution of C65 by means of rGO (HC-rGO-5 electrode) enhances the electronic conductivity allowing targeting for higher charge storage, especially at high applied current densities where electric conductivity becomes critical. At the lowest frequency region (below 1 Hz) ion diffusion through the material gives the Warburg impedance (Z_w), fitted using a diffusion resistance and a pseudo-capacitance (C_{int}) representing the non-ideal finite diffusional behavior at lowest frequencies. This is commonly observed as a 45° straight line respect the y-axis and it is mostly similar for both electrodes.

Finally, different LICs were assembled facing either HC or HC-rGO-5 electrodes with previously reported olive pit derived AC in a 1:1 mass ratio. In order to study the system at its maximum performance, both electrodes were preconditioned. Thus, HC-rGO-5 was cycled five times between 0.005–2 V vs. Li⁺/Li at C/10 rate in order to form a SEI layer and supply sufficient lithium to compensate the first cycle irreversibility and then, a cut-off potential of 0.2 V vs. Li⁺/Li was set in order to avoid any lithium plating. Similarly, the AC was charged to a cut-off potential of 4.2 V vs. Li⁺/Li. Fig. 6a shows the

GA charge/discharge potential profiles of HC-rGO-5 and AC-based electrodes vs. Li⁺/Li together with the overall HC-rGO-5//AC hybrid cell performance at different current densities (Fig. S1 shows the HC//AC system for comparison). At a first glance, both cell and electrode profiles in the HC-rGO-5//AC system look the same, despite the increasingly applied current density, suggesting that faster operation is not altering the supercapacitor behavior of the overall cell. In more detail, through a decreasing discharge time from 60 min to 5 min and to further 20 seconds, the charge/discharge profile of the LIC is absolutely symmetric in all cases, typical of supercapacitors. This indicates that the capacitive mechanism taking place at the positive electrode (i.e. AC) is governing the overall cell response profile at all the studied charge/discharge rates. Moreover, comparing both HC vs. HC-rGO-5 electrodes (Fig. S1 vs. Fig. 6a), it can be observed that the addition of rGO onto the HC electrode keeps the negative electrode potential sweep narrower (~ 0.7 V vs. ~ 1.1 V), owing to its faster operation capabilities and the voltage drop of the system at high rates is noticeably lower. The impact of rGO into the overall cell performance is also clearly visible within the energy-to-power ratios given in the Ragone Plot in Fig. 6b. Building a HC//AC LIC already implies a substantial gain in the energy performance as compared to the analogue olive pit derived AC//AC EDLC system. On a further step, the substitution of the commonly added conductive carbon (SuperC65)

by the as-prepared rGO boosted the energy of the LIC system -which was cycled in the standard operating 1.5 V–4.2 V cell voltage- far beyond. The latter delivers an energy density of 130 Wh kg⁻¹AM at 150 W kg⁻¹AM while the energy of the benchmark LIC is limited to 100 Wh kg⁻¹AM at 150 W kg⁻¹AM, what implies an increase of 30%. Nevertheless, this low power region can still be covered by fast batteries in cost of their cycling life or fabrication cost due to the need of oversizing the systems, or either building micro-batteries. However, within 1 minute discharge time, that is, a purely EDLC region where no battery can operate, the newly developed LIC is able to deliver an improved 95 Wh kg⁻¹AM at 5500 W kg⁻¹AM compared to the more modest 72 Wh kg⁻¹AM at 4200 W kg⁻¹AM ratio of the benchmark LIC (Fig. 6c). At the very high power region (discharge times within seconds), i.e. 10 kW kg⁻¹AM, HC-rGO-5 based LIC provides an energy density as high as 82 Wh kg⁻¹AM, 60% and 85% larger than the energy provided by the benchmark LIC and the EDLC system respectively. Furthermore, the use of rGO allows targeting even higher power ratios than the EDLC itself, reaching an outstanding value of 60 Wh kg⁻¹AM at 20 kW kg⁻¹AM. This result highlights the need of a fast battery-type negative electrode able to give response to such high power demands. In terms of durability, cyclability was tested at 10 A g⁻¹ (t_{discharge} = 9 seconds), reaching to a highly appealing 88% capacitance retention after 10000 cycles (Fig. S2).

In view of the excellent performance of the overall LIC and the incomplete usage of the HC-rGO-5 potential window vs. Li⁺/Li along the applied 1.5–4.2 V window, an extended LIC voltage window of 1–4.2 V was also tested in order to make a major use of the HC-rGO-5 electrode and find the limits of the system. Fig. S3 (extended 1–4.2 V) show that the HC-rGO-5 can stand the extended voltage window without almost altering its potential sweep or slightly widening it toward lower potentials, while the AC potential window positively swings by ~2.6 V instead of the narrower ~2 V sweep in the 1.5–4.2 V cell voltage. The extended window allows optimizing the device performance by achieving the widest potential window of both electrodes without decomposing the electrolyte while maximizing the capacity of both electrodes. As can be seen in Fig. 6b and Fig 6c, the energy density gain is substantial, reaching the highly challenging 200 Wh kg⁻¹AM at 150 W kg⁻¹AM value at low power rates while getting close to 100 Wh kg⁻¹AM at 10 kW kg⁻¹AM, to our knowledge, one of the best reported energy-to-power ratios ever reported for a dual carbon LIC. Cyclability of the system remains unaffected maintaining about 85% capacitance retention at 10000 cycles.

Conclusions


In this work we have developed an ultrafast hard carbon electrode by adding graphene in the electrode formulation. Impedance analysis reveals that formed 3D interpenetrating network of graphene enables faster ion diffusion and electron transport owing to a reduced charge-transfer and charge-transport resistances. Thus, the newly developed HC-rGO-based electrode presents double the capacity at high cycling rates with respect to the bare HC electrode, reaching a capacity of 162 mAh g⁻¹ at 10C. This fact enables the fabrication of LICs able to reach outstanding energy density values of 200 Wh kg⁻¹AM at low power rates and 60 Wh kg⁻¹AM at an extremely demanding power peak of 20 kW kg⁻¹AM with a 88% capacitance retention after 10000 cycles.

Acknowledgments

We thank the European Union (Graphene Flagship, Core 2, grant number 785219), the Spanish Ministry of Science and Innovation (MICINN/FEDER) (RTI2018-096199-B-I00) and the Basque Government (Elkartek 2018) for the financial support of this work. M. Arnaiz thanks the Spanish Ministry of Science, Innovation and Universities for her FPU pre-doctoral fellowship (FPU15/04876).

ORCID

Jon Ajuria  <https://orcid.org/0000-0003-0480-4877>

María Arnaiz  <https://orcid.org/0000-0001-8800-0643>

References

1. L. Zhang R.Liu, X. Sun, H. Liu, and J. Zhang, *Electrochemical technologies for energy storage and conversion.*, Wiley, Germany, 2012.
2. H. Wang, C. Zhu, D. Chao, Q. Yan, and H. J. Fan, Nonaqueous hybrid lithium-ion and sodium-ion capacitors, *Adv Mater.*, **46** (2017).
3. G. G. Amatucci, F. Badway, A. Pasquier, and T. Zheng, An asymmetric hybrid non-aqueous energy storage cell, *J. Electrochem. Soc.*, **148**, 930 (2001).
4. T. Aida, K. Yamada, and M. Morita, An advanced hybrid electrochemical capacitor that uses a wide potential range at the positive electrode, *Electrochem. Solid-State Lett.*, **9**, 534 (2006).
5. <http://www.jmenergy.co.jp/en/profile.html>, November, 2017.
6. D. P. Dubal, O. Ayyad, V. Ruiz, and P. Gómez-Romero, Hybrid energy storage: the merging of battery and supercapacitor chemistries, *Chem. Soc. Rev.*, **7**, 1777 (2015).
7. R. Väli, A. Jänes, T. Thomborg, and E. Lust, Synthesis and characterization of D-glucose derived nanospheric hard carbon negative electrodes for lithium- and sodium-ion batteries, *Electrochim. Acta.*, **253**, 536 (2017).
8. H. Yu, X. Dong, Y. Pang, Y. Wang, and Y. Xia, High power lithium-ion battery based on spinel cathode and hard carbon anode, *Electrochim. Acta.*, **228**, 2551 (2017).
9. X. Sun, X. Zhang, H. Zhang, N. Xu, K. Wang, and Y. Ma, High performance lithium-ion hybrid capacitors with pre-lithiated hard carbon anodes and bifunctional cathode electrodes, *J. Power Sources*, **270**, 318 (2014).
10. S. Jayaraman, A. Jaina, M. Ulaganathan, E. Edison, M. P. Srinivasan, R. Balasubramanian, V. Aravindan, and S. Madhavi, Fabrication of high energy Li-ion capacitors from orange peel derived porous carbon, *Chem. Eng. Process*, **316**, 5051 (2017).
11. J. Ni, Y. Huang, and L. Gao, A high-performance hard carbon for Li-ion batteries and supercapacitors application, *J. Power Sources*, **223**, 306 (2013).
12. E. Buiel and J.R. Dahn, Reduction of the irreversible capacity in hard carbon anode materials prepared from sucrose for Li-ion batteries, *J. Electrochem. Soc.*, **145**, (1998).
13. V. Simone, A. Boulineau, A. de Geyer, D. Rouchon, L. Simonin, and S. Martinet, Hard carbon derived from cellulose as anode for sodium ion batteries: Dependence of electrochemical properties on structure, *J. Energy Chem.*, **25**, 761 (2016).
14. Y. Bai, Z. Wang, C. Wu, R. Xu, F. Wu, Y. Liu, H. Li, J. Lu Y.Li, and K. Amine, Hard carbon originated from polyvinyl chloride nanofibers as high-performance anode material for Na-ion battery, *Appl. Mater. Interfaces*, **7**, 5598 (2015).
15. E. M Lotfabad, J. Ding, K. Cui, A. Kohandehghan, W. P. Kalisvaart, M. Hazelton, and D. Mitlin, High-density sodium and lithium ion battery anodes from banana peels, *ACS Nano*, **8**, 71158 (2014).
16. T. Zhang, J. Mao, X. Liu, M. Xuan, K. Bi, X. Zhang, J. Hu, J. Fan, S. Chen, and G. Shao, Pinecone biomass-derived hard carbon anodes for high-performance sodium-ion batteries, *RSC Advances*, **66**, 41504 (2017).
17. W. Lv, F. Wen, J. Xiang, J. Zhao, L. Li, L. Wang, Z. Liu, and Y. Tian, Peanut shell derived hard carbon as ultralong cycling anodes for lithium and sodium batteries, *Electrochim. Acta.*, **176**, 533 (2015).
18. P. Liu, Y. Li, Y. Hu, H. Li, L. Chen, and X. Huang, A waste biomass derived hard carbon as a high-performance anode material for sodium-ion batteries, *J. Mater. Chem. A*, **34**, 13046 (2016).
19. E. Irisarri, N. Amini, S. Tennison, C. Matei Ghimbeu, J. Gorka, C. Vix-Guterl, A. Ponrouch, and M. R. Palacin, *J. Electrochem. Soc.*, **165**, A4058 (2018).
20. Y. Zhu, L. Yang, X. Zhou, Feng Li, J. Wei, and Z. Zhou, Boosting the rate capability of hard carbon with an ether-based electrolyte for sodium ion batteries, *J. Mater. Chem. A*, **20**, 9528 (2017).
21. M. Arnaiz, V. Nair, S. Mitra, and J. Ajuria, Furfuryl alcohol derived high-end carbons for ultrafast dual carbon lithium ion capacitors, *Electrochimica Acta.*, **304**, 437 (2019).
22. E. de la Llave, V. Borgel, E. Zinigrad, F-F. Chesneau, P. Hartmann, Y.-K. Sun, and D. Aurbach, Study of the most relevant aspects related to hard carbons as anode materials for Na-ion batteries, compared with Li-ion systems, *Isr. J. Chem.*, **55**, 1260 (2015).
23. W. J. Cao, J. F. Luo, J. Yan, X. J. Chen, W. Brandt, M. Warfield, D. Lewis, S. R. Yturriaga, D. G. Moya, and J. P. Zheng, High Performance Li-Ion Capacitor Laminate Cells Based on Hard Carbon/Lithium Stripes Negative Electrodes, *J. Electrochem. Soc.*, **164**, A93 (2017).
24. J. Ajuria, E. Redondo, M. Arnaiz, R. Mysyk, T. Rojo, and E. Goikolea, Lithium and sodium ion capacitors with high energy and power densities based on carbons from recycled olive pits, *J. Power Sources*, **359**, 17 (2017).
25. F. Su, C. You, Y. B He, W. Lv, a W. Cui, a F. Jin, a B. Li, b Q.-H Yang, and F. Kang, Flexible and planar graphene conductive additives for lithium-ion batteries, *J. Mater. Chem.*, **20**, 9644 (2010).
26. H. Liu, P. Gao, J. Fang, and G. Yang, LiV(PO₄)₃/graphene nanocomposites as cathode material for lithium ion batteries., *Chem. Commun.*, **47**, 9110 (2011).
27. X. Zhang, S. Han, C. Fan, L. Li, and W. Zhang, Hard carbon enveloped with graphene networks as lithium ion battery anode, *Mater. Lett.*, **138**, 259 (2015).
28. P. Alvarez C.Botas, C. Blanco, R. Santamaría, M. Granda, P. Ares, F. Rodríguez-Reinoso, and R. Menéndez, The effect of the parent graphite on the structure of graphene oxide, *Carbon*, **50**, 275 (2012).
29. H. C. Schniepp, J. L. Li, M. J. McAllister, H. Sai, M. Herrera-Alonso, D. H. Adamson, R. K. Prud'homme, R. Car, D. A. Saville, and I. A. Aksay, Functionalized single

- graphene sheets derived from splitting graphite oxide, *J. Phys. Chem. B*, **110**, 8535 (2006).
30. B. A. Boukamp, A nonlinear least squares fit procedure for analysis of impedance data of electrochemical systems, *Solid State Ionics*, **20**, 31 (1986).
 31. C. Botas, P. Álvarez, P. Blanco, M. Granda, C. Blanco, R. Santamaría, L. J. Romasanta, R. Verdejo, M. A. López-Manchado, and R. Menéndez, Graphene materials with different structures prepared from the same graphite by the Hummers and Brodie methods, *Carbon*, **65**, 156 (2013).
 32. N. Morimoto, T. Kubo, and Y. Nishina, Tailoring the Oxygen Content of Graphite and Reduced Graphene Oxide for Specific Applications, *Sci. Rep.*, **6** (2016).
 33. V. H. Nguyen and H. B. Gu, LiFePO₄ batteries with enhanced lithium-ion-diffusion ability due to graphene addition, *J. Appl. Electrochem*, **10**, 1153 (2014).
 34. D. A. Stevens and J. R. Dahn, The mechanisms of lithium and sodium insertion in carbon materials, *J. Electrochem. Soc.*, **148**, 803 (2001).
 35. D. Aurbach, M. D. Levi, E. Levi, and A. Schechter, Failure and stabilization mechanisms of graphite electrodes, *J. Phys. Chem. B*, **101**, 2195 (1997).
 36. D. Aurbach, M. D. Levi, E. Levi, and H. Teller, The structure of a 3 V Li_xMnO₂ cathode and its change upon electrochemical lithiation, *J. Electrochem. Soc.*, **145**, 3440 (1998).
 37. M. D. Levi, G. Salitra, B. Markovsky, H. Teller, D. Aurbach, U. Heider, and L. Heider, Solid-state electrochemical kinetics of Li-ion intercalation into Li_{1-x}CoO₂: simultaneous application of electroanalytical techniques SSCV, PITT, and EIS, *J. Electrochem. Soc.*, **146** (1999).
 38. A. Funabiki, M. Inaba, Z. Ogumi, S. Yuasa, J. Otsuji, and A. Tasaka, Impedance study on the electrochemical lithium intercalation into natural graphite powder, *J. Electrochem. Soc.*, **145**, 172 (1998).
 39. T. Doi, K. Miyatake, Y. Iriyama, T. Abe, Z. Ogumi, and T. Nishizawa, Lithium-ion transfer at an electrolyte/non-graphitizable carbon electrode interface, *Carbon*, **42**, 3183 (2004).
 40. I. Belharouak, Lithium ion batteries-new developments, InTech, 2012.
 41. R. Marassi, F. Nobili, F. Croce, and B. Socratì, Electronic and electrochemical properties of Li_xNi_{1-y}Co_yO₂ cathodes studied by impedance spectroscopy, *Chem Mater.*, **13**, 1642 (2001).
 42. F. Nobili, S. Dsoke, F. Croce, and R. Marassi, Correlation of AC-impedance and in situ X-ray spectra of LiCoO₂, *J. Phys. Chem. B*, **110**, 11310 (2006).
 43. M. Zarrabeitia, F. Nobili, M. A. Muñoz-Márquez, T. Rojo, and M. Casas-Cabanas, Composition and evolution of the Solid-Electrolyte Interphase in Na₂Ti₃O₇ electrodes for Na-ion batteries: XPS and Auger parameter analysis, *J. Power Sources*, **330**, 7801 (2016).